Air-flow sensitive hairs: boundary layers in oscillatory flows around arthropod appendages

T. Steinmann[1], J. Casas[1,*], G. Krijnen[2] and O. Dangles[1]

[1]Institut de Recherche sur la Biologie de l'Insecte–UMR CNRS 6035, Faculté des Sciences et Techniques, Université François Rabelais, Parc de Grandmont Avenue Monge, 37200 Tours, France and [2]MESA+ Research Institute, Transducers Science and Technology group Faculty of Electrical Engineering, University of Twente, PO Box 217, 7500 AE Enschede, The Netherlands

*Author for correspondence (e-mail: jerome.casas@univ-tours.fr)

Summary

The aim of this work is to characterize the boundary layer over small appendages in insects in longitudinal and transverse oscillatory flows. The problem of immediate interest is the early warning system in crickets perceiving flying predators using air-flow-sensitive hairs on cerci, two long appendages at their rear. We studied both types of oscillatory flows around small cylinders using stroboscopic micro-particle image velocimetry as a function of flow velocity and frequency. Theoretical predictions are well fulfilled for both longitudinal and transverse flows. Transverse flow leads to higher velocities than longitudinal flow in the boundary layer over a large range of angles between flow and cylinder. The strong spatial heterogeneity of flow velocities around filiform-shaped appendages is a rich source of information for different flow-sensing animals. Our results suggest that crickets could perceive the direction of incoming danger by having air-flow-sensitive hairs positioned around their entire cerci. Implications for biomimetic flow-sensing MEMS are also presented.

Key words: viscous boundary layer, hair biomechanics, cercal system, cricket, flow sensing, sensor design.

Introduction

Boundary flows have been studied in a biological context for several decades, including fish swimming (Anderson et al., 2001), crustacean and moth olfaction (Koehl et al., 2001; Stacey, 2002) and fluid sensing in arthropods in air and water (Humphrey et al., 1993; Barth et al., 1993; Devarakonda et al., 1996; Humphrey et al., 2003a; Humphrey et al., 2003b). Air-flow sensing using filiform hairs partially immersed in the boundary layer around the body has been extensively studied in arthropods, especially in spiders and crickets (Shimozawa and Kanou, 1984; Humphrey and Devarakonda, 1993; Barth et al., 1993). Filiform hairs are among the most sensitive biological sensors in the animal kingdom (Shimozawa et al., 2003). These outstanding sensitive structures are used to detect approaching animals, in particular the oscillatory signals produced by the wing beats of prey and predators (Tautz and Markl, 1979; Barth et al., 1993; Gnatzy and Heusslein, 1986). According to the body of work performed to date, a variation of hair length is assumed to allow spiders and crickets to fractionate both the intensity and frequency range of an air flow signal.

The biomechanics of hair movement in an oscillating fluid has stimulated extensive research during the last few decades, and several models have been developed (Fletcher, 1978; Shimozawa and Kanou, 1984; Humphrey and Devarakonda, 1993). In all these models, a hair is defined as an inverted pendulum with a rigid shaft supported by a spring at its base. This mechanical model can be described by four parameters (Shimozawa et al., 2003; Humphrey et al., 2003): the moment of inertia that represents the mass distribution along the hair shaft; the spring stiffness which provides the restoring torque towards the resting position; the torsional resistance within the hair base; and the coupling resistance between the hair shaft and the air (see Appendix).

An important assumption of these models concerns the nature of the oscillating flow in the boundary layer over the cerci, as it greatly impacts the movement of hairs of different lengths. The boundary layer has been theoretically predicted and often experimentally confirmed on large structures for both longitudinal and transverse oscillatory flows (Raney et al., 1954; Bertelsen et al., 1973; Williamson, 1985; Obasaju et al., 1988; Justesen, 1991; Tatsuno and Bearman, 1990). These studies were, however, conducted for Reynolds and Strouhal numbers very different from those of biological relevance, with the exception of the studies by Holtsmark et al. (Holtsmark et al., 1954) and Wang (Wang, 1968). While the longitudinal flow

over arthropod appendages has been thoroughly characterised by Barth et al. (Barth et al., 1993), the transverse flow has been much less studied. Barth et al. characterized the boundary layer in longitudinal and transverse flows using laser Doppler anemometry (LDA) over a spider leg (Barth et al., 1993). However, only a few measurements were carried out and they were limited by the 300 μm resolution of the LDA system, hence missing out the region nearest to the substrate. Moreover, the influence of the source orientation on the boundary layer was not investigated.

The aim of the present work is to characterize, in a systematic way in terms of phase and frequency, the boundary layer over small antenna-like appendages in crickets in an oscillatory flow for both longitudinal and transverse flows. Situated at the rear end of crickets, these appendages of conical shape, called cerci, are equipped with hundreds of filiform hairs of varying length. We use stroboscopic micro-particle image velocimetry (μPIV) to carry out measurements on artificial cerci placed in oscillatory flows of varying frequencies and orientations with respect to the source. Thus, our work deals with the flow around a cricket cercus, and not with the flow around a single hair. Our results are compared to existing models for longitudinal and transverse flows. We discuss the implications of our findings in terms of hair length and angular hair location around the cercus to extract as much information as possible. The perspectives are in terms of cricket perception of attacking predators and in terms of biomimetic Micro-Electric-Mechanical Systems (MEMS) flow sensors.

Materials and methods
Air flow modelling around a cylinder

The signal emitted by a flying predator can be approximated by a spherical point source radiating an isotropic sinusoidal wave in all directions (Tautz and Markl, 1979) [see Sueur et al. (Sueur et al., 2005) for finer distinctions in the near-field region]. The far-field velocity of air particles is described by the equation:

$$U_\infty(t) = U_0 \sin(\omega t) , \qquad (1)$$

where U_0 is the flow oscillation amplitude, and ω is the angular frequency (rad s^{-1}), with $\omega = 2\pi f$, f being the frequency of flow oscillations (s^{-1}). A signal impacting the cylinder from any angle can be decomposed into longitudinal (V_l), radial (V_r) and circumferential (V_θ) components (Fig. 1A).

We first consider a flow oscillating parallel to a cylinder (longitudinal flow). To avoid end effects, the length of the cylinder (L) is supposed to be much larger than its diameter, D ($L > 10D$). Under these conditions, the fluid velocity at time (t) can be expressed as a function of the distance to the cylinder (y) as follows:

$$V_l(t,y) = U_0 \left(\sin(\omega t) - \frac{\sin(\omega t - \beta y)e^{-\beta y}}{\left(1 + \frac{2y}{D}\right)^{\frac{1}{2}}} \right) , \qquad (2)$$

where $\beta = (\omega/2\nu_{air})^{\frac{1}{2}}$ is the border effect factor (m^{-1}), $\nu_{air} = \mu_{air}/\rho_{air}$ is the kinematic viscosity of the fluid (m^2 s^{-1}), μ_{air} is the dynamic viscosity of the fluid (Ns m^{-2}), ρ_{air} is the density of the fluid (kg m^{-3}) and D is the diameter of the cylinder (m) (Humphrey and Devarakonda, 1993).

Due to the viscosity effect, there is a phase displacement, φ, with the distance from the cylinder:

$$\varphi(y) = \arctan \left(\frac{\exp(-\beta y)\sin(\beta y)}{\sqrt{\frac{D+2y}{D}} - \exp(-\beta y)\cos(\beta y)} \right) . \qquad (3)$$

Second, we consider the flow oscillating perpendicular to a cylinder, theoretically described by Holtsmark et al. (Holtsmark et al., 1954). We compared our results to the first degree of this analytical approximation as we are interested in a simple semi-analytical solution of the Navier Stokes equation for modelling hair movement. This first-order solution corresponds to the oscillatory part of the solution. The circumferential component of the flow velocity, V_θ, triggers hair defection. The cylinder represents a cercus, not a hair on a cercus. This circumferential component is:

$$V_\theta(\theta,y,t) = -U_0 \sin\theta \left\{ -\left(1 - \frac{(D/2)^2}{(y+D/2)^2} C_r\right) \sin\omega t + \right.$$
$$\left. (X_r - Z_r)\sin\omega t + \left(X_i - Z_i + \frac{(D/2)^2}{(y+D/2)^2} C_i\right)\cos\omega t \right\}, \qquad (4)$$

with

$$X = \frac{H_0(\epsilon y)}{H_0\left(\epsilon \frac{D}{2}\right)}, \; Y = \frac{H_1(\epsilon y)}{H_0\left(\epsilon \frac{D}{2}\right)}, \; Z = \frac{H_2(\epsilon y)}{H_0\left(\epsilon \frac{D}{2}\right)}, \; C = Z\left(\frac{D}{2}\right) . \qquad (5)$$

X, Y, Z, C are complex numbers with X_i, Y_i, Z_i, C_i and X_r, Y_r, Z_r, C_r being their imaginary and real parts, respectively. H_n is the Hankel function of the first kind (Abramowitz and Stegun, 1965), y is the distance to the substrate (m), D is the diameter of the cylinder (m), $\epsilon = [i(\omega/\nu)]^{\frac{1}{2}}$, and θ is the angle between the cylinder and the flow (rad). The radial component of the flow, which is parallel to the hair and has no influence on its motion, is expressed as follows:

$$V_r(\theta,r,t) = U_0 \cos\theta \left\{ -\left(1 + \frac{(D/2)^2}{(y+D/2)^2} C_r\right) \sin\omega t + \right.$$
$$\left. (X_r + Z_r)\sin\omega t - \left(X_i + Z_i - \frac{(D/2)^2}{(y+D/2)^2} C_i\right)\cos\omega t \right\}, \qquad (6)$$

Eqns 4 and 6 show the existence of a phase lag δ between V_r and V_θ. This phase lag δ is given by:

$$\tan(\sigma - \delta) = \frac{-X_i + Z_i - \frac{(D/2)^2}{r^2} C_i}{1 - \frac{(D/2)^2}{r^2} C_r - X_r + Z_r} , \qquad (7)$$
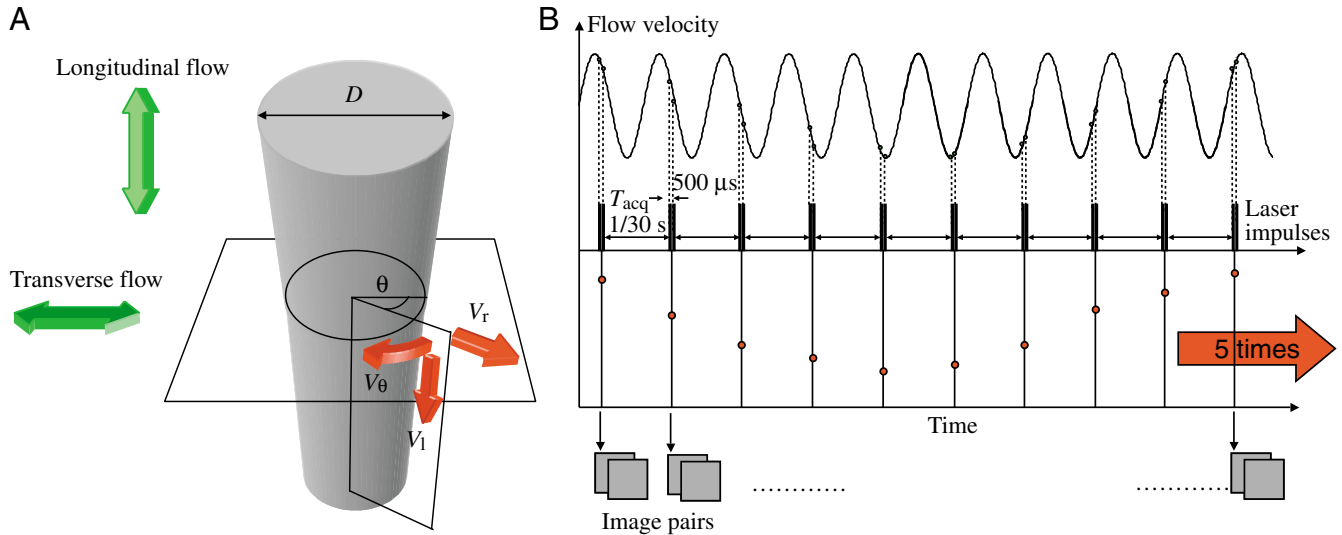
Fig. 1. (A) Longitudinal, circumferential and radial components of an oscillating flow acting on a hair perpendicular to a cylindrical substrate. (B) Principle of stroboscopic measurement of a flow oscillating at high frequency with a low-frequency sampling device. In this example, we take pairs of images (separated by 500 μs) at a frequency of 30 Hz of a flow oscillating at 33 Hz. The pseudo time increment is 3 ms and we need 10 pairs to sample a full period of the flow oscillations. We repeat this procedure five times and proceed then to a phase average.

σ being given by:

$$\tan(\sigma) = \frac{X_i + Z_i - \dfrac{(D/2)^2}{r^2}\, C_i}{X_r + Z_r - 1 - \dfrac{(D/2)^2}{r^2}\, C_r} \cdot \qquad (8)$$

Therefore, the fluid far from the cylinder oscillates along a straight line whereas the fluid near the cylinder oscillates in an elliptic fashion (Holtsmark et al., 1954). We solved numerically the phase advance of V_θ with distance from the cylinder.

Experimental set-up

We used cylinders (D=1 mm, L=40 mm) made of steel, of identical base diameter but of a longer length than in real animals. This enabled us to avoid boundary effect at both extremities. These cylinders were stiff. They were held by a microManipulator placed in a way to avoid vibrations produced by the loudspeakers.

Flow measurements were performed using two-dimensional PIV. It is now well established that PIV and LDA techniques are suitable for acoustical measurement (Campbell et al., 2000). Recently, these techniques have been used to characterize the laminar acoustic viscous boundary layer and the acoustic streaming in tube and wave guide (Castrejón-Pita et al., 2006). Artificial cylinders were placed in a cylindrical glass container (L=200 mm, D=100 mm), with two loudspeakers (40 W, 5 Ω; SP 45/4; Monacor, Brême, Germany) at both ends, connected to a sinusoidal signal generator (2 MHz; TG 230; Thurlby-Thandar, Huntingdon, Cambs, UK).

We checked for signal integrity at all frequencies in the centre of the container using an LDA system (FlowLite 1D 65X90; Dantec Dynamics A/S, Skovlunde, Denmark). At the central point, $U(\omega t)=U_0\sin(\omega t)$, with amplitude U_0=35 mm s^{-1}. The loudspeaker delivered good signals from 25 Hz upwards. Measurements were conducted at 25°C corresponding to an air kinematic viscosity, ν_{air}=1.56×10^{-5} m^2 s^{-1}. The air inside the sealed glass box was seeded with 0.2 μm oil particles (Di-Ethyl-Hexyl-Sebacat, 0.5 L; TPAS, Dresden, Germany) using an aerosol generator (ATM 230; ACIL, Chatou, France). The laser of the PIV illuminated the flow produced by the wave through the glass (NewWave Research Solo PIV 2, 532 nm, 30 mJ, Nd:YAG, dual pulsed; Dantec Dynamics A/S). The laser sheet (width=17 mm, thickness at focus point=50 μm) was operated at low power (3 mJ at 532 nm) to minimize glare. A target area was then imaged onto the CCD array of a digital camera (Photron FastCam X1280 PCI 4K) using a stereomicroscope (LEICA M13, X10) that produced a 2×2 mm window around the substrate. In order to measure high-frequency and low-amplitude oscillatory movements, we set the CCD to capture a light pulse at 30 Hz in separate image frames every 500 μs, with a laser impulsion length of 4±1 ns (Fig. 1B). To reduce undesirable reflections, the cylinders were covered with fluorescent paint, which re-emits the light of the laser at another wavelength. We used a narrow band filter working at the laser wavelength λ=532 nm placed under the camera. Measurements were conducted for velocities U_0=35 mm s^{-1}, within the range of airborne vibration amplitude generated 10 cm in front of a flying predatory wasp (Tautz and Markl, 1979). Flow frequencies ranged from 30 to 180 Hz. For a cylinder diameter of 1 mm, the corresponding peak Reynolds number (*Re*) is 1.6 and the Strouhal numbers (*St*) range from 2.7 to 16.2.

Stroboscopic measurements

We used the stroboscopic principle to sample high-frequency sinusoidal signals (ranging from 30 Hz to 180 Hz)

with a PIV system limited to 30 Hz (Schram and Riethmuller, 2001). As explained in Fig. 1B, this consists of sampling a signal of period f_{flow} with a frequency (f_{acq}) slightly lower than a sub-multiple of the signal frequency. This technique gives us the following pseudo sampling time interval (t_{strob}):

$$t_{strob} = \mathrm{mod}\,(T_{acq}, T_{flow})\,, \qquad (9)$$

where T_{acq} is the inverse of the PIV sampling frequency, and T_{flow} is the inverse of the signal frequency. The number of sampling points, N, covering a full period of the signal is given by:

$$N = (T_{flow} / t_{strob})\,. \qquad (10)$$

A numerical example is given in the legend of Fig. 1B. In a second example, let us assume we sample a 119 Hz signal at 30 Hz. The pseudo time interval is then $t_{strob}=0.28$ ms, corresponding to a phase of $\omega t_{strob}=0.2$ rad$=0.06\pi$ rad, giving $N=33$ sampling points per full period of signal. We repeated this measurement five times and proceeded to a phase average on the basis of 50 and 150 pair images in the first and second example, respectively. The estimation of the signal phase φ corresponding to each sample point is obtained through inference, not measurements. The known far-field velocity U_∞ and local velocity U_0 are used with the relationship $\varphi=\arcsin(U_\infty/U_0)$.

Data acquisition

Flow measurements for both longitudinal and transverse flows were conducted for six frequencies (30, 60, 90, 120, 150 and 180 Hz). The two-dimensional (2-D) velocity vector fields were derived from sub-sections of the target area of the particle-seeded flow by measuring the movement of particles between two light pulses. Images were divided into small subsections (width, 70 μm; resolution, 32×32 pixels; covering rate, 50%) and cross-correlated with each other using a flow map software (Flow Manager 4.4; Dantec Dynamics A/S). The correlation produced a signal peak, identifying the common particle displacement. An accurate measurement of the displacement (and thus of the velocity) was achieved with sub-pixel interpolation.

We averaged five vector fields for each phase of the signal. For longitudinal flows, velocity profiles were obtained by averaging point measurements over 2 mm along the cylinder. For transverse flows, the velocity profile was extracted at five different angles (90, 60, 45, 30 and 15°) but not averaged along the length of the cylinder.

With subsection windows of 32×32 pixels, it is possible to obtain valid measurements down to 0.1 pixels (Mayinger and Feldman, 2001). In our set-up, this corresponds to 0.3 mm s^{-1}, equivalent to 1% of U_0.

Results

Frequency

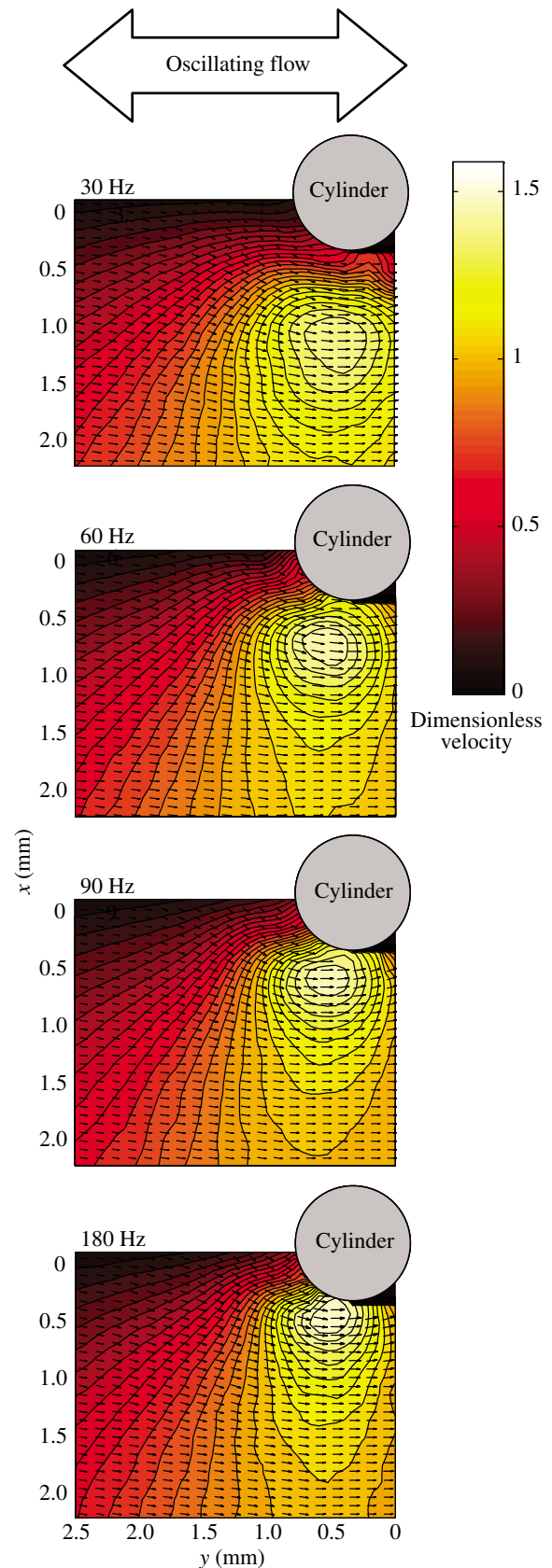Fig. 2 shows the frequency dependence of the velocity around a cylinder in transverse flow. It represents the

Fig. 2. Vector field of velocity amplitude around a cylinder of 1 mm diameter at four frequencies in transverse flow. Vectors are of constant length.

amplitude of the flow, i.e. the difference between the maximum velocity fields [measured at $\omega t=(\pi/2)$] and the minimum velocity fields [measured at $\omega t=-(\pi/2)$]. The boundary layer thickness around the cylinder is significantly reduced at high frequencies. From these measurements, we extracted the velocity profiles for five different circumferential θ angles (90, 60, 45, 30 and 15°) (Fig. 3), an angle θ of 0° being directly upwind. As predicted by theory, the flow velocity profiles vary as a function of the sine of this angle. At 30°, the curvature effects of the cylinder produce a noticeable peak in flow velocity, increasing at higher angles and levelling off at 90°. Maximal velocities also increase with flow frequency, from $1.4U_0$ at 30 Hz to $1.6U_0$ at 180 Hz.

In longitudinal flow, we measured significant changes in fluid velocity at a short distance above the cylinder (<0.5 mm) as a function of flow oscillation frequency (Fig. 3, grey line). For longitudinal flow, the velocity profiles match nicely with those predicted by theory both in terms of amplitude and distance of the maximal velocity above the cylinder. Measurements very close (70 μm) to the surface of the cylinder are ~50% higher than theoretical values. We do not know if it is due to a PIV uncertainty or a failing of the theory. The high light intensity in the focalisation part of the laser light sheet, which is then very near to the substrate, may heat the surface, leading to an increase of velocity (Brownian motion). The thickness of the boundary layer decreases with increasing flow frequency, as predicted by the theory.

The 90° and the 60° transverse flows produce higher velocities than the longitudinal one throughout the entire profile. This pattern is also observed for the 45° transverse flow but only within the first 1000 μm above the cylinder for a 30 Hz flow and within the first 700 μm for a 180 Hz flow. For all frequencies, the 30° and the 15° profiles are smaller than the longitudinal one, and the 45° profile is greater than the longitudinal one along the first 300 μm.

Phasing

Fig. 4 represents the temporal evolution of the velocity field around a cylinder in a transverse flow. The circulating zones typical of oscillatory flows are clearly visible. Particles trapped in this region rotate in antiphase on both sides of the cylinder (red arrows in Fig. 4). This is due to the interplay between their circumferential components, which are moving in phase, and their radial components, which are out of phase by $\pi/2$. We extracted the velocity profiles of the circumferential component of flow around the cylinder from the data represented in Fig. 4 and plotted them in Fig. 5. Hair movement, which we did not measure, is induced by this component. The phase is constant for each value of θ and is a function of y. Fig. 5 also shows the evolution of the velocity profile over a cylinder with time for a longitudinal flow. We obtained a good agreement between theory and measurement except at very small distances (<90 μm).

The phase displacement with distance from the cylinder is represented in Fig. 6. The fit with the theory is good. Phase displacement goes from $\pi/4$ close to the surface to 0 rad at the
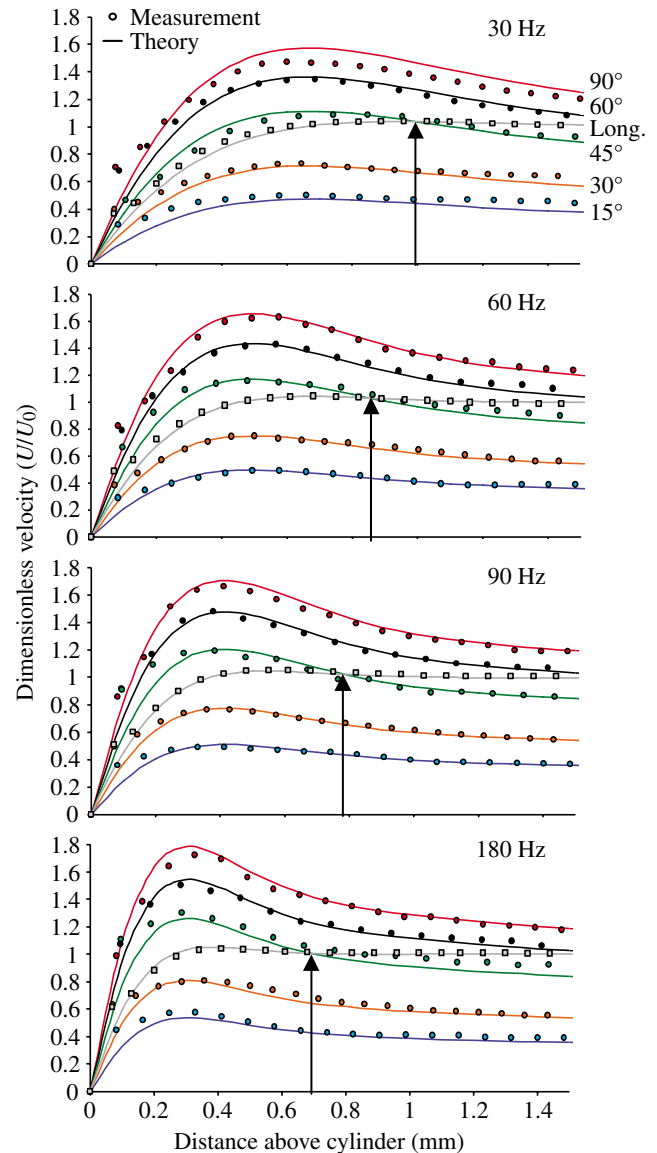

Fig. 3. Velocity profiles for longitudinal and transverse flows at four frequencies around a cylinder of 1 mm diameter. Holtsmark solutions for transverse flow (lines) and particle image velocimetry (PIV) measurements (points) at angles of 90° (red circles), 60° (black circles), 45° (green circles), 30° (orange circles) and 15° (blue circles). Humphrey solution for longitudinal flow (grey line) and corresponding PIV measurement (squares). The distance above the cylinder at which both components are equal is highlighted (arrow).

largest distances. There is therefore a phase advancement in the boundary layer. While the observed changes in amplitude between transverse and longitudinal flows are important, there is almost no phase lag between them.

Discussion

Measurements versus models

This PIV study is one of the most comprehensive regarding flow velocities around cylinders of small diameters in
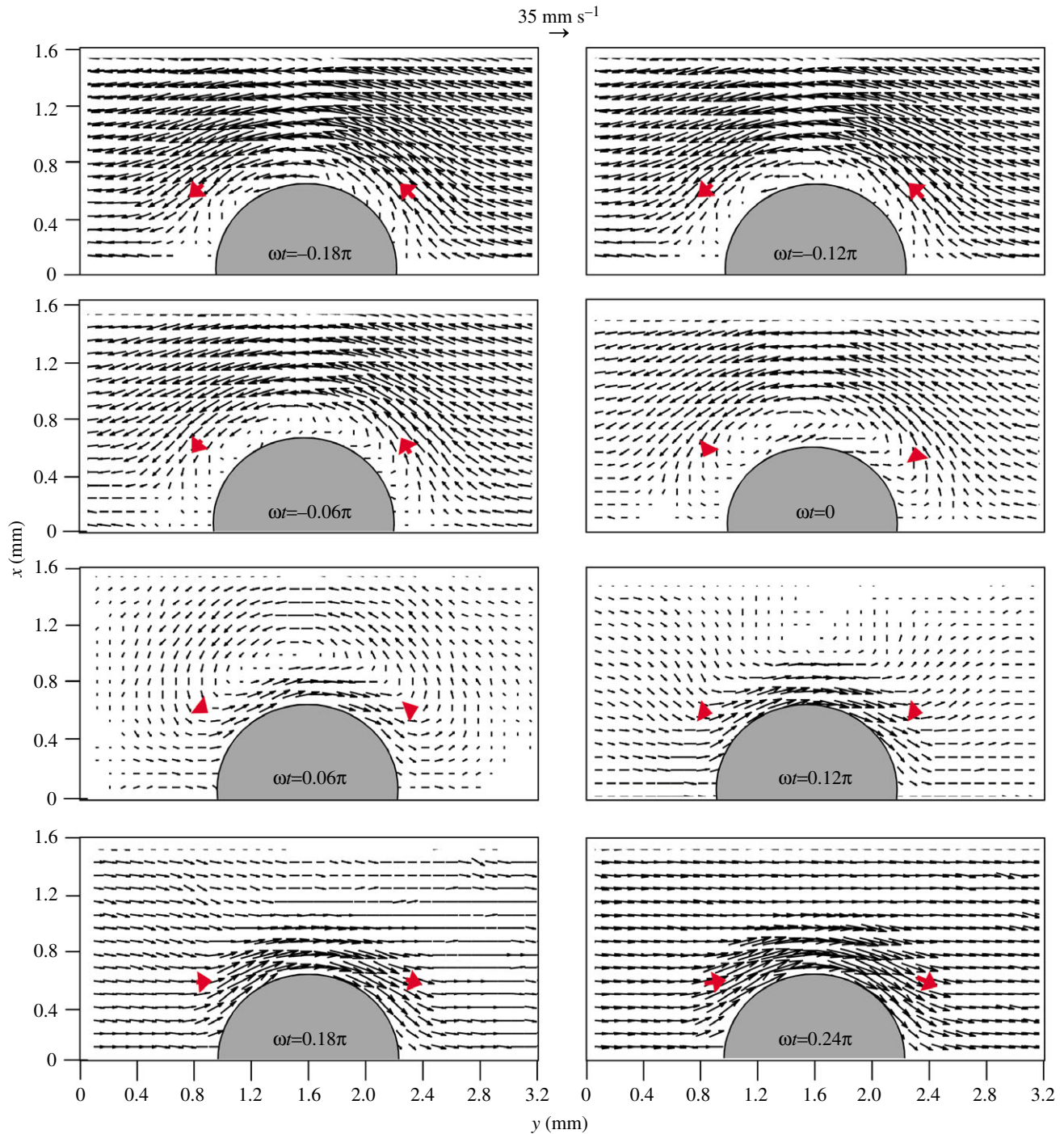
Fig. 4. Temporal evolution of the velocity field around a cylinder of 1 mm diameter in a 120 Hz transverse flow. The phase interval separating each vector field is 0.06 rad.

oscillatory flows at low *Re*. We could not use the approximation developed by Wang (Wang, 1968) and later used by Humphrey and Devarakonda [equation A.2.1 (Humphrey et al., 1993)] as the conditions for its application [$Re \times St \gg 1$ and $(Re/St) \ll 1$] did not apply for the full range of values we were interested in, particularly for the low frequencies [$Re \times St = 3$ and $(Re/St) = 0.4$ for $f=30$ Hz]. By contrast, the Holtsmark et al. model (Holtsmark et al., 1954)

gives meaningful predictions over the full range of parameters. An exploration of the predictions of these different models indicates that the model of Wang, and its refinement by Humphrey et al., is valid from 180 Hz down to 90 Hz, but deteriorates at lower frequencies. As mentioned before, we compared the transverse measurement to the first approximation solution. The streaming motion to the hair movement was confirmed by visual examination of the film
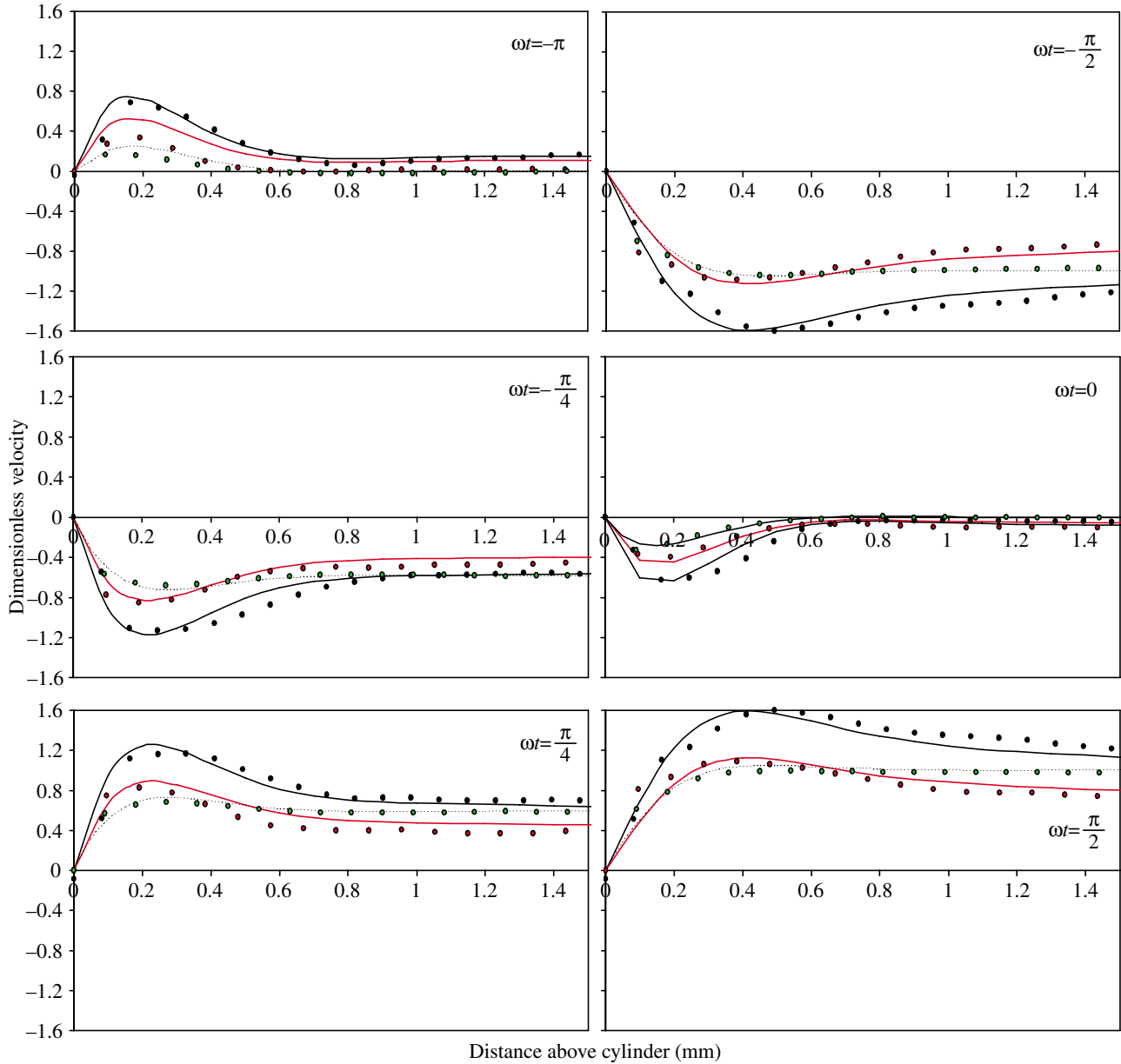
Fig. 5. Temporal evolution of the instantaneous velocity in longitudinal and transverse flows over a cylinder of 1 mm diameter at 120 Hz. Humphrey solution for longitudinal flow (dotted line) and particle image velocimetry (PIV) measurement (grey circles). Holtsmark solutions for transverse flow (lines) and PIV measurements (points) at angles of 90° (red circles) and 45° (black circles).

taken with the PIV camera, but we neglected it as its amplitude was estimated to be 2.5% of the amplitude of the far-field oscillatory flow (Holtsmark et al., 1954; Raney et al., 1954).

The match between model predictions for both longitudinal and transverse flows and experimental data is very good, except for the smallest measured distance from the cylinder. Reasons for this lack of fit may originate either from a breakdown of the many approximations made in the models or from experimental errors, as their weight is large at those small velocities. The slightest misalignment of the thin laser sheet with the tiny cylinder can indeed produce such a mismatch. Our

results confirm the pioneer results obtained by Barth et al. (Barth et al., 1993) regarding the relative velocities in longitudinal and transverse flows around spider legs. In particular, these authors observed that velocities would be stronger in transverse flow than in longitudinal flow. We observed higher velocities for transverse flow as long as the θ angle is between 60° and 120°. As was previously predicted (Humphrey et al., 1993), the profiles are also quite different, transverse flows producing local velocities up to 1.6 times stronger than the far-field values. By contrast, the maximal amplification of the far-field value is only 1.1 for longitudinal flows.

on their bottom portion and are submitted to the far-field velocity over most of their remaining length. These far-field velocities decline with decreasing angle θ, so that the transverse drag torque acting on a long hair will also decline with decreasing angle and become inferior to the longitudinal one for an angle θ of 57°. Short hairs experiencing similar air flow are totally immersed in the boundary layer. The decline of transverse flow velocity with the angle is lower in the boundary layer, so that transverse drag torque will be higher than longitudinal drag torque over a larger range of θ angles, down to 37°.

What are the consequences in terms of hair sensitivity as measured by the maximal amplitude of hair displacement? Whatever its position around the cylinder, a long hair shows high displacement values at low frequency. Hair displacement amplitude sharply declines from 80 Hz and reaches a negligible value at frequencies above 500 Hz (Fig. 8A). By contrast, short hairs do not show such strong frequency-dependent behaviour over the values of interest (Fig. 8B). For the air velocity and frequency used in Figs 7 and 8, the influence of the transverse component is greater than that of the longitudinal component in the angle interval of [90°, 50°] for long hairs. This interval is further extended to [90°, 37°] for short hairs. Thus, short hairs are more sensitive than long hairs to the transverse component of flow from almost any direction. This result
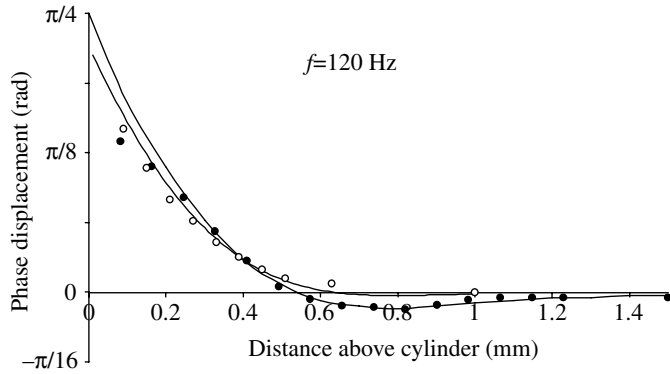

Fig. 6. Phase shift between far field and boundary layer flow as a function of distance from the cylinder at 120 Hz. Analytical solution (Eqn 3) of the phase displacement (dotted line) and particle image velocimetry (PIV) measurement (open circles) for a longitudinal flow. Numerical solution (line) and PIV measurement (filled circles) for a transverse flow at a circumferential angle of 90°.

Implications for air-flow sensing in animals and MEMS

The strong spatial heterogeneity of flow velocities around appendages in transverse flow is a rich source of information for flow-sensing animals, in particular for those using flow-sensing hairs. A single hair submitted to an air flow from any angle will experience longitudinal and transverse forces over its entire length. The relative importance of these air flow components will be a function of circumferential location θ and hair length. We distinguish between long (1500 µm) and short (300 µm) hairs in the following discussion, as they are known to differ in best-tuned frequencies and represent two extreme situations. We computed the drag torque (see Appendix) in order to understand the relative influence of the longitudinal and transverse components of any flow on hairs of different lengths (Fig. 7), the virtual mass torque being almost negligible. Long hairs experience boundary layer effects only
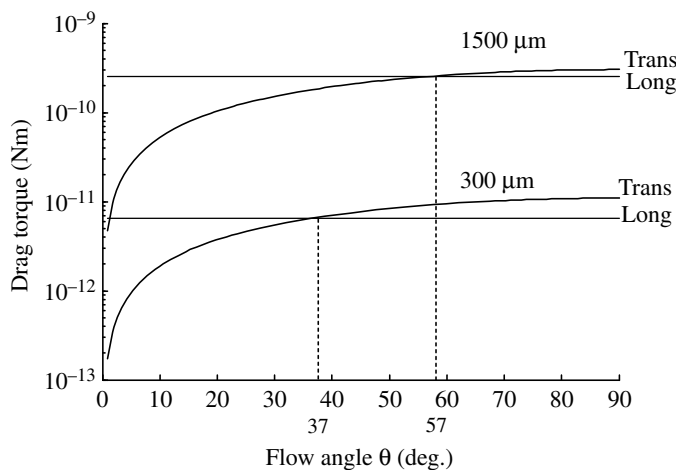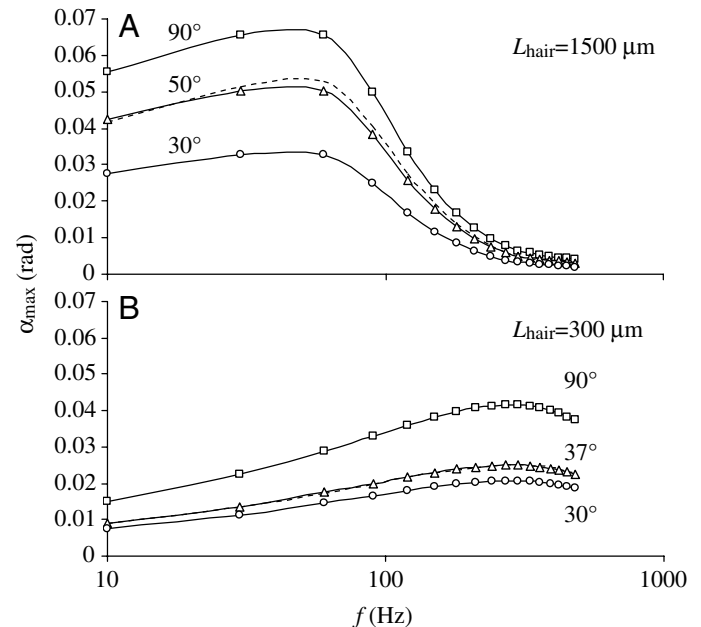

Fig. 8. Maximal hair displacement as a function of flow frequency (f_{flow}) and circumferential angle (θ). (A) Maximal hair displacement of long hairs positioned on a cylinder of 1 mm diameter, for attack angles of 90° (squares, transverse flow), 50° (triangles), 30° (circles) and 0° (broken line, longitudinal flow). (B) Maximal hair displacement of short hairs positioned on a cylinder of 1 mm diameter, for impact angles of 90° (squares, transverse flow), 37° (triangles), 30° (circles) and 0° (dotted line, longitudinal flow). For both computations, U_0=35 mm s^{-1}.

Fig. 7. Viscous drag torque for short and long hairs in transverse and longitudinal flows. Flow oscillations, f=120 Hz; flow velocity, V=35 mm s^{-1}; hair lengths, 1500 µm and 300 µm.

makes sense physically, as the largest differences between longitudinal and transverse flows are in the boundary layer, in which the small hairs are totally immersed. These considerations were tested at other frequencies (30 Hz and 180 Hz) and were found to be quite robust.

Our results have important implications for hair canopy arrangement in arthropods using air flow to sense prey or predators. First and foremost, the spatially heterogeneous information provided by a transverse flow around a cylinder implies that hairs should be placed all around a cylinder, maximising the chances to perceive a source coming from any angle. Indeed, an isotropic distribution of hairs ensures that some hair will always be perpendicular to the flow, thereby experiencing the smallest possible boundary layer, and hence the largest possible displacement. For similar reasons, hairs of the same length vibrate with different amplitudes around a cylinder depending on their radial location. Arthropods may therefore perceive the direction of an incoming air flow in a differentiated manner using the radial distribution of the canopy, very much as their hair lengths act as a Fourier transform for frequency decomposition through different natural frequencies. This directionality filter may help crickets to identify the direction of the approaching source.

The rich content of information in the spatially heterogeneous flow around a cylinder has escaped the attention of previous workers, who cited the great computational advantages of considering a cylinder of low curvature as a plate for the purpose of computation of hair movement. We now need to revisit both the hair biomechanical models and the neurocomputational models of danger perception in crickets on the basis of these results. Cricket air flow sensors have recently been a source of inspiration to build artificial air flow sensors (Dijkstra et al., 2005). Design guidelines for building flow-sensing MEMS arrays were also based on biomimetic ideas borrowed from the cricket's cerci. A spatial arrangement of MEMS hairs with a large range of angles relative to flow direction on a dedicated platform would increase the sensitivity of such sensors by a large margin. Such design could represent a major advance to the actual mounting, on a horizontal plate, of MEMS hairs restricted to measuring longitudinal flows. This is however not a trivial task in MEMS fabrication.

List of symbols

d	hair diameter
D	cylinder diameter
f_{acq}	PIV sampling frequency
f_{flow}	oscillating air flow frequency
$F_D(y,t)$	drag per hair unit length acting at height y
$F_{VM}(y,t)$	added mass force per hair unit length acting at height y
H_n	Hankel function of the first kind
I	moment of inertia
I_h	hair moment of inertia
I_{VM}	moment of inertia of the added mass stagnating around and moving with the hair
L	cylinder length
$L(t)$	angular momentum
L_{hair}	hair length
N	number of sampling points
R	damping factor including frictional terms at the hair base
R_{VM}	damping factor due to the friction between added mass of fluid moving with the hair and surrounding air
S	spring stiffness
t	time
t_{strob}	pseudo sampling time interval
T_{acq}	inverse of the PIV sampling frequency
T_D	drag torque
T_{flow}	inverse of the signal frequency
T_R	damping torque
T_S	restoring torque
T_{VM}	torque associated with the virtual mass of fluid
U_∞	far-field velocity
U_0	flow oscillation amplitude
$V_F(y,t)$	velocity acting on the hair
V_l	longitudinal component of a flow impacting the cylinder
V_r	radial component of a flow impacting the cylinder
V_θ	circumferential component of a flow impacting the cylinder
X,Y,Z,C	complex numbers
X_i,Y_i,Z_i,C_i	imaginary parts of the complex numbers X,Y,Z,C
X_r,Y_r,Z_r,C_r	real parts of the complex numbers X,Y,Z,C
y	distance to the cylinder
α	angular deflection of the hair with respect to its equilibrium orientation
β	border effect factor
δ	phase lag between V_r and V_θ
γ	Euler's constant
λ	laser wavelength
μ_{air}	dynamic viscosity of air
ν_{air}	kinematic viscosity of air
ρ_{air}	air density
ρ_{hair}	hair density
θ	angle between the cylinder and the flow
ω	angular frequency
φ	phase displacement

Appendix

Hair movement modelling

The physical behaviour of a single hair submitted to an air flow can be modelled by the equation given by Shimozawa and Kanou (Shimozawa and Kanou, 1984a) and modified by Humphrey et al. (Humphrey et al., 1993). Most of this information is also contained in Magal et al. (Magal et al., 2006). For a rigid hair oscillating relative to a fixed axis of

rotation, conservation of angular momentum, $L(t)$, states that the rate of change of angular momentum is equal to the sum of torques acting on the hair:

$$\frac{dL(t)}{dt} = I \frac{d^2\alpha}{dt^2} = T_D(t) + T_{VM}(t) - T_R(t) - T_S(t) , \quad (A1)$$

where I is the moment of inertia of the hair relative to the axis of rotation and α is the angular deflection of the hair with respect to its equilibrium orientation. The drag torque, T_D, arises due to frictional drag acting along the hair shaft. The torque T_{VM} is associated with the virtual mass of fluid, which at any instant must be also accelerated along with the hair. The damping torque, T_R, arises at the rotation point of the hair and results from frictions between the hair base and the surrounding cuticle. The restoring torque, T_S, is equivalent to spring stiffness, expressing the elasticity of the socket membrane, and arises at the rotation point of the hair. The velocity profiles are integrated in the first two torques, which drive hair motion, whereas the last two torques are always opposed to hair deflection.

Hair's moment of inertia

According to Humphrey et al. (Humphrey et al., 1993) and Kumagai et al. (Kumagai et al., 1998), the total inertial moment of a filiform hair, I (Nm s^{-2} rad^{-1}), is given by:

$$I = I_h + I_{VM} , \quad (A2)$$

where I_h is the hair moment of inertia:

$$I_h = \frac{\pi \rho_{hair} d^2}{48} \left[L_{hair} \left(4L_{hair}^2 + \frac{3d^2}{4} \right) \right] , \quad (A3)$$

where d is hair diameter (m), L_{hair} is hair length (m), and ρ_{hair} is hair density (kg m^{-3}). I_{VM} represents the moment of inertia of the added mass of the fluid stagnating around and moving with the hair of constant diameter and is given by Humphrey et al. (Humphrey et al., 1993) as:

$$I_{VM} = \frac{-\pi \mu G L_{hair}^3}{6gf_{flow}} + \frac{\pi \rho d^2 L_{hair}^3}{12} . \quad (A4)$$

Stokes (Stokes, 1851) shows that for values of the dimensionless parameter:

$$s = \frac{d}{4} \left(\frac{2\pi f_{flow}}{\nu_{air}} \right)^{\frac{1}{2}} , \quad (A5)$$

such that $s \ll 1$:

$$G = \frac{-g}{g^2 + \left(\frac{\pi}{4} \right)^2} , \quad (A6)$$

with:

$$g = y + \ln(s) , \quad (A7)$$

where γ (dimensionless) is Euler's constant, d is hair diameter (m) at height y above the cercus, f is the oscillating air flow frequency (Hz), and ν_{air} is the air kinematic viscosity (m^2 s^{-1}).

Fluid-induced drag and added mass torques

The fluid-induced instantaneous drag and added mass torques are obtained by integrating the fluid-induced drag and added mass forces per unit length acting along the total length of the hair, L_{hair} (m):

$$T_D(t) = \int_0^L F_D(y,t)y \, dy , \quad (A8)$$

$$T_{VM}(t) = \int_0^L F_{VM}(y,t)y \, dy , \quad (A9)$$

where y is the position along the hair (m), and $F_D(y,t)$ and $F_{VM}(y,t)$ are the drag and added mass forces per hair unit length, acting at height y, respectively. Eqns A8 and A9 state that the total torque that acts to deflect the hair from its resting position is given by the integrated sum of all torques over the arm length of rotation y. Each of the torques is generated on an infinitesimally thin disc of the hair shaft. Theoretical expressions for F_D and F_{VM}, applicable to a fluid oscillating perpendicular to a hair, have been derived by Stokes (Stokes, 1851) and previously used in filiform hair modelling studies (Humphrey et al., 1993; Shimozawa et al., 1998).

Drag and added mass forces per unit length

For a fluid oscillating perpendicular to a cylindrical hair segment, the drag force acting on the cylinder at height y above the cercus surface is:

$$F_D(y,t) = 4\pi \mu G V_F(y,t) , \quad (A10)$$

where μ is the fluid dynamic viscosity (kg m^{-1} s^{-1}), G is given by Eqn A6 and $V_F(y,t)$ is the velocity acting on the hair.

The added mass force per unit length is given by:

$$F_{VM}(y,t) = \frac{-\pi \mu G \dfrac{dV_F(y,t)}{dt}}{2gf_{flow}} + \pi \rho \left(\frac{d}{2} \right)^2 \frac{dV_F(y,t)}{dt} , \quad (A11)$$

where G is given by Eqn A6 and g is given by Eqn A7.

Damping torque

This torque results in part from the friction between the hair base and the surrounding cuticle (Shimozawa and Kanou, 1984a; Shimozawa et al., 1998). The damping factor (Nm s^{-1} rad^{-1}) includes frictional terms at the hair base (R) as well as friction between added mass of fluid moving with the hair and surrounding air (R_{VM}). Both sources of torque always act so as to oppose hair motion. The total damping torque, T_R (N m^{-1}), is given by:

$$T_R(t) = (R + R_{VM}) \frac{d\alpha(t)}{dt} , \quad (A12)$$

where R (Nm s^{-1} rad^{-1}), is a constant damping factor which is allometrically related to L_{hair} (μm) (Shimozawa et al., 1998):

$$R = 2.88 \times 10^{-14} (L_{hair}/1000)^{2.77} , \quad (A13)$$

and R_{VM} is the damping factor due to the friction between added mass of fluid moving with the hair and surrounding air:

$$R_{VM} = 4\pi\mu G\,(L_{hair}{}^3/3)\,. \tag{A14}$$

Restoring torque

The socket joint membrane acts as a spring, causing a restoring torque that always acts to oppose hair motion:

$$T_S(t) = S\alpha(t)\,, \tag{A15}$$

where S (Nm rad^{-1}) is the spring stiffness, which is allometrically related to L_{hair} (μm) (Shimozawa et al., 1998):

$$S = 1.9\times10^{-11}\,(L_{hair}/1000)^{1.67}\,. \tag{A16}$$

References

Abramowitz, M. and Stegun, I. A. (ed.) (1965). *Handbook of Mathematical Functions* (*National Bureau of Standards*, *Applied Mathematics Series No. 55*). Washington: Dover Publications.

Anderson, E. J., McGillis, W. R. and Grosenbaugh, M. A. (2001). The boundary layer of swimming fish. *J. Exp. Biol.* **204**, 81-102.

Barth, F. G., Wastl, U., Humphrey, J. A. C. and Devarakonda, R. (1993). Dynamics of arthropod filiform hairs. II. Mechanical properties of spider trichobothria (Cupiennius salei Keys.). *Philos. Trans. R. Soc. Lond. B Biol. Sci.* **340**, 445-461.

Bertelsen, A., Svardal, A. and Tjøtta, S. (1973). Nonlinear streaming effects associated with oscillating cylinders. *J. Fluid Mech.* **59**, 493-511.

Campbell, M., Cosgrove, J.-A., Greated, C.-A., Jack, S. and Rockliff, D. (2000). Review of LDA and PIV applied to the measurement of sound and acoustic streaming. *Opt. Laser Tech.* **32**, 629-639.

Castrejón-Pita, J. R., Castrejón-Pita, A. A., Huelsz, G. and Tovar, R. (2006). Experimental demonstration of the Rayleigh acoustic viscous boundary layer theory. *Phys. Rev. E* **73**, 036601.

Devarakonda, R., Barth, F. and Humphrey, J. A. C. (1996). Dynamics of arthropod filiform hairs. IV: Hair motion in air and water. *Philos. Trans. R. Soc. Lond. B Biol. Sci.* **351**, 933-946.

Dijkstra, M., van Baar, J. J., Wiegerink, R. J., Lammerink, T. S. J., de Boer, J. H. and Krijnen, G. J. M. (2005). Artificial sensory hairs based on the flow sensitive receptor hairs of crickets. *J. Micromech. Microeng.* **15**, 132-138.

Fletcher, N. H. (1978). Acoustical response of hair receptors in insects. *J. Comp. Physiol.* **127**, 185-189.

Gnatzy, W. and Heusslein, R. (1986). Digger wasp against crickets. I. Receptors involved in the antipredator strategies of the prey. *Naturwissenschaften* **73**, 212-215.

Holtsmark, J., Johnsen, I., Sikkeland, T. and Skavlem, S. (1954). Boundary layer flow near a cylindrical obstacle in oscillating incompressible fluid. *J. Acoust. Soc. Am.* **26**, 26-39.

Humphrey, J. A. C. and Devarakonda, R. (1993). Dynamics of arthropod filiform hairs. I. Mathematical modelling of the hair and air motions. *Philos. Trans. R. Soc. Lond. B Biol. Sci.* **340**, 423-444.

Humphrey, J. A. C., Devarakonda, R., Iglesias, I. and Barth, F. G. (1993). Dynamics of arthropod filiform hairs. I. Mathematical modelling of the hair and air motions. *Philos. Trans. R. Soc. Lond. B Biol. Sci.* **340**, 423-440.

Humphrey, J. A. C., Barth, F. G. and Voss, K. (2003a). The motion-sensing hairs of arthropods: using physics to understand sensory ecology and adaptive evolution. In *Ecology of Sensing* (ed. F. G. Barth and A. Schmid), pp. 105-115. Berlin, Heidelberg, New York: Springer-Verlag.

Humphrey, J. A. C., Barth, F. G., Reed, M. and Spak, A. (2003b). The physics of arthropod medium-flow sensitive hairs: biological models for artificial sensors. In *Sensors and Sensing in Biology and Engineering* (ed. F. G. Barth, J. A. C. Humphrey and T. Secomb), pp. 129-144. Berlin, Heidelberg, New York: Springer Verlag.

Justesen, P. (1991). A numerical study of oscillating flow around a circular cylinder. *J. Fluid Mech.* **222**, 157-196.

Koehl, M. A. R., Koseff, J. R., Crimaldi, J. P., Cooper, T., McCay, M., Wiley, M. B. and Moore, P. A. (2001). Lobster sniffing filters the spatio-temporal information in a turbulent odour plume. *Science* **294**, 1948-1951.

Kumagai, T., Shimozawa, T. and Baba, Y. (1998). The shape of windreceptor hairs of cricket and cockroach. *J. Comp. Physiol. A* **183**, 187-192.

Magal, C., Dangles, O., Caparroy, P. and Casas, J. (2006). Hair canopy of cricket sensory system tuned to predator signals. *J. Theor. Biol.* **241**, 459-466.

Mayinger, F. and Feldman, O. (2001). *Optical Measurements: Techniques and Applications* (2nd edn.). Berlin, Heidelberg, New York: Springer-Verlag.

Obasaju, E. D., Bearman, P. W. and Graham, J. M. R. (1988). A study on forces, circulation and vortex patterns around a circular cylinder in oscillatory flow. *J. Fluid Mech.* **196**, 467-494.

Raney, W. P., Corelli, J. C. and Westervelt, P. J. (1954). Acoustic streaming in the vicinity of a cylinder. *J. Acoust. Soc. Am.* **26**, 1006-1014.

Schram, C. and Riethmuller, M. L. (2001b). Evolution of vortex ring characteristics during pairing in an acoustically excited jet using stroboscopic particle image velocimetry. *4th International Symposium on Particle Image Velocimetry (PIV'01)*, Göttingen, 17–19 September, paper 1157.

Seur, J., Tuck, L. and Robert, D. (2005). Sound radiation around a flying fly. *J. Acoust. Sci. Amer.* **118**, 530-538.

Shimozawa, T. and Kanou, M. (1984). The aerodynamics and sensory physiology of range fractionation in the cercal filiform sensilla of the cricket Gryllus bimaculatus. *J. Comp. Physiol. A* **155**, 495-505.

Shimozawa, T., Kumagai, T. and Baba, Y. (1998). Structural scaling and functional design of the cercal wind-receptor hairs of cricket. *J. Comp. Physiol. A* **183**, 171-186.

Shimozawa, T., Murakami, J. and Kumagai, T. (2003). Cricket wind receptors: thermal noise for the highest sensitivity known. In *Sensors and Sensing in Biology and Engineering* (ed. F. G. Barth, J. A. C. Humphrey and T. Secomb), pp. 145-157. Berlin, Heidelberg, New York: Springer Verlag.

Stacey, M. T., Mead, K. S. and Koehl, M. A. R. (2002). Molecule capture by olfactory antennules: mantis shrimp. *J. Math. Biol.* **44**, 1-30.

Stokes, G. G. (1851). On the effect of the internal friction of fluids non the motion of pendulums. *Math. Phys. Pap.* **3**, 1-141.

Tatsuno, M. and Bearman, P. W. (1990). A visual study of the flow around an oscillating cylinder at low Keulegan-Carpenter number and low Stokes numbers. *J. Fluid Mech.* **211**, 157-182.

Tautz, J. and Markl, H. (1979). Caterpillars detect flying wasps by hairs sensitive to airborne vibration. *Behav. Ecol. Sociobiol.* **4**, 101-110.

Wang, C. (1968). On high-frequency oscillatory viscous flows. *J. Fluid Mech.* **32**, 55-68.

Williamson, C. H. K. (1985). Sinusoidal flow relative to circular cylinders. *J. Fluid Mech.* **155**, 141-174.